Journal of Advanced Research in Applied Sciences and Engineering Technology

Journal homepage:
https://semarakilmu.com.my/journals/index.php/applied_sciences_eng_tech/index
ISSN: 2462-1943

Improvement of Power Quality Using Reduced Switch Count Eleven-Level Inverter in Smart Grid

Ch. Santosh Kumar[1,*], S. Tara Kalyani[2]

[1] Department of Electrical and Electronics Engineering, BVRIT Hyderabad College of Engineering for Women, Hyderabad, India
[2] Department of Electrical and Electronics Engineering, Jawaharlal Nehru Technological University Hyderabad, Hyderabad, India

ARTICLE INFO

Article history:
Received 1 April 2023
Received in revised form 24 May 2023
Accepted 25 May 2023
Available online 13 June 2023

Keywords:
Photovoltaic, Power Demand, Cascaded Multilevel Inverter, Utility Grid, DC to DC Converters, DC Link Voltages, Reduced Switch

ABSTRACT

This article proposed a hybrid control topology to cascaded multilevel-inverter (CMLI) using 11-level for the grid-tied photovoltaic generation system. The proposed hybrid technique combines an archerfish hunting optimiser (AHO) and Spike Neural Network (SNN); hence, it is called the AHO-SNN technique. The proposed control technique is to maintain the regulation of power or maximal energy conversion of the solar subsystem and reduce total harmonic distortion (THD). Here, the AHO is utilised to construct the optimum control signal dataset. The best control signals are estimated using a data set performed by SNN. The resultant control signals will regulate insulated-gate-bi-polar-switches (IGBT) of Cascaded MLI. The proposed AHO-SNN control topology determines the converter switching states by constructing the operating modes of the generation system. The system parameter changes and outside disturbances are optimally minimised with this control strategy. The proposed AHO-SNN control is done in MATLAB platform, and it evaluated their performance by using existing methods, like War Strategy Optimization Algorithm (WSO) Fuzzy Wavelet Neural Network (FWNN), Side-Blotched Lizard Algorithm (SBLA), Adaptive Neuro-Fuzzy Inference System (ANFIS), and Memetic Fire-Fly Algorithm (MFA). The result shows that the proposed approach based on THD is less than existing approaches.

1. Introduction

In recent decades, while dealing with fossil-fuel usage and issues of carbon dioxide-emission to electric vehicles (EVs), renewable energy production methods, new energy-saving technologies, and advanced consumer electronics have been rapidly produced [1]. Due to its sustainable, clean and less polluted aspects, PV energy is greatly valued [2]. To achieve maximal PV power usage [3], maximal power-point-tracking (MPPT) is a mandatory function of the photovoltaic power system. Many maximal power-point-tracking algorithms, like incremental conductance (INC) and the perturbation-and-observation (P&O), approaches [5], are broadly accepted. Apart from this, to recognise the MPPT, a dc-to-dc converter and the pulse-width-modulation (PWM) method must be

* *Corresponding author.*
E-mail address: chksantosh@yahoo.com

https://doi.org/10.37934/araset.31.1.1433

linked to the photovoltaic array [6]. Nabae [7] suggested Multilevel Inverters (MLI), initiated with the neutral-point-clamped-inverter methodology. Due to their advantages over traditional three-level PWM inverters, MLIs have recently been more appealing to researchers [8]. Compared to the conventional H-bridge inverters, MLI has two major benefits [9] and decreases the output waveform's harmonic composition because of multi-dc phases and the greater voltage capability. [10]. Because of the devices' decreased voltage stresses (dv/dt) favour the multilevel inverter in great power medium voltage applications [11]. The MLI includes a topological configuration, which permits preferred output voltage to be integrated, either isolated or interconnected, into 3 major types, like flying-capacitor multilevel inverter, disconnected dc sources, and diode-clamped MLI [12]. Sub-bridge dc bus voltages were combined with preserving a ternary asymmetric ratio with the major bridge by choosing the appropriate set of space vectors [13]. The discovery of [14] space-vector terminations aids in achieving the natural balancing of capacitor voltages [15], allowing for inverter modulation. The number of bridges to be stacked [16] is based on conditions like the convergence permissible time, count of switching devices, satisfactory [17] measures of power quality, etc. [18]. Output voltages theoretical analysis is offered and experimentally proved [19]. Also, both stage and line voltages with less THD to the modulation system can produce. [20]

2. Recent Research Work: A Brief Review

Different research works have earlier existed in the literature that depended on the MLI with hybrid renewable energy sources with different approaches and features. Here, a few were revised as the single dc source per phase. Vasu *et al*. [21] have introduced the 3-phase ternary-asymmetric cascaded H-bridge MLI (CHBMLI) topology. Among the H-bridges, one was fed from a dc-source, and the remaining were derived from the floating capacitors and their dc links. To improve an asymmetric ternary rate with the major bridge by choosing the correct set-of-space-vectors for the dc-bus voltages of sub-bridges were integrated. The inverter modulation was performed by exploring the space-vector redundancies to achieve the capacitor voltage's natural balance. Choosing the bridge count was cascaded based on conditions like convergence permissible time, satisfactory power quality indices, number of switching devices, etc. Satish Kumar and Sasi Kumar have executed the 3-phase hybrid-network connection system that depends on CMI in a smart hybrid method for the modelling and controller design. Wolf Pack Search (WPS) aided the Recurrent Neural Network (RNN), a hybrid method called the WPSNN method. Here, the 3-phase CMI controller system was regarded as 2-phase and studied using a smart controller. First, Wolf Pack Search was established to determine the net photovoltaic and wind voltages. Second, Wolf Pack Search aided to RNN was utilised to separate the reference network currents. The multilevel inverter was popular for industrial and commercial uses, and it was introduced recently by M.Tayyab et al. Here, presented a power flow control and an eleven-level inverter. The overall price of the inverter decreased the devices because of the provided topology and provided a lower component number than other topologies. This inverter consists of six bidirectional switches, 2 DC sources, two capacitors and 14 quadrant switches for the voltage divider circuit. Among the hybrid energy network and the power storing modules for managing power conversions, Amarnath and Sujatha have developed a management system. These were structured to meet load supplies. By utilising an optimised Iterative-cuckoo-optimization was attained a maximum power point (MPP). The incorporated controller was modelled to optimise performance for moving power from the hybrid system to loaded and discharged flows.

The recent review depends on the power quality development of photovoltaic and multilevel inverter systems, which shows that power quality is important. Here, the inverter is a tool to transfer DC energy into the AC that grids and loads need. It is a crucial and significant component of

power conversion in renewable energy. The expensive and substantial low-pass filters are employed before supplying power to the utility grid because the inverter's output has high harmonic content. Moreover, due to switching losses and high-voltage stress, these are not being used in high-power applications. Multilevel inverters (MLI) were developed as the best alternative for medium and high-power applications. The three conventional MLI topologies are diode-clamped MLI (DC-MLI), Flying-capacitor MLI (FC-MLI), and cascaded H-bridge MLI (CHB-MLI). The primary characteristics of MLIs include: performing both PWM at basic and high switching frequencies, resulting in output waveforms with less harmonic distortion (HD). The drawback is the need for numerous power switches, which makes the system big and adds complexity. This obstacle has been tackled using an MLI topology with fewer switches. Some methods like Particle-Swarm-Optimization (PSO), Genetic Algorithm, and Fuzzy address the power quality problem of photovoltaic systems and multilevel MLI. The fuzzy logic controller requires several pieces of data. It is equally effective for programs of all sizes, regardless of past data. The main disadvantages of genetic algorithms are extremely slow processing speeds and the inability to identify the best solution. Hence the main objective is to reduce total harmonic distortion in the smart grid using a cascaded multilevel inverter.

3. Structure of Proposed Cascaded MLI for Reduce the Total Harmonic Distortion in Smart Grid

Configuration of the Cascaded MLI reduced-switch 11-level inverter for the grid-tied photovoltaic system is depicted in Figure 1. The level of MLI is 11, and it is attached to the load and source. The PV is attached to a DC-to-DC converter for extracting the maximal power. The proposed method regulates the current and voltage and decreases the system harmonics. The Cascaded MLI method is used to supply the signal of control, and it is linked to pulse width modulation. The gate driver supplies the switching pulse of the multilevel inverter by utilising the PWM pulses. The hybrid AHO-SNN strategy is proposed to lower the harmonic system. The SNN is used to anticipate the ideal control signals, while the AHO generates the system's control signal.

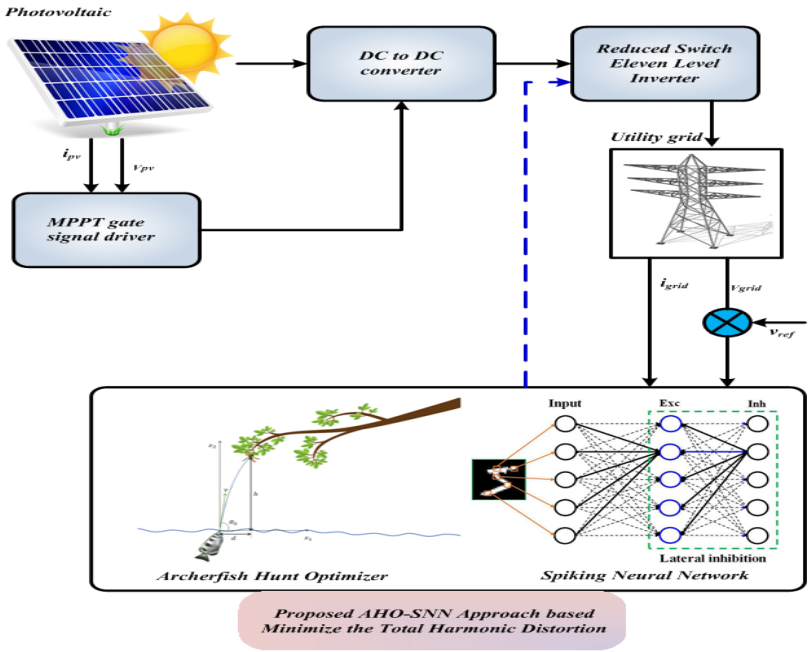

Fig. 1. Configuration of Cascaded MLI reduced-switch 11-level inverter for grid-tied photovoltaic System

3.1 Model of MLI

The multilayer inverter converts power on multiple-voltage steps to attain higher power quality and high voltage capability. The serial connection for a multilevel bridge topology makes up the MLI. The multilevel inverter's standard output voltage is,

$$v_{o/p} = v_{o/p}^{1} + v_{o/p}^{2} + \cdots v_{o/p}^{n} \tag{1}$$

The inverter's level of voltage count is,

$$N_s = 2n + 1 \tag{2}$$

The n Level-inverters' maximum output voltage is,

$$v_{out}^{max} = n * v_{dc} \tag{3}$$

For *n* level inverter, the steps for the quantity of voltage are as follows,

$$\text{For} j = 1,2,\ldots.n,\ N_s = \begin{cases} 2^{n+1} - 1 if v_j = 2^{j-1} v_{dc} \\ 3^n if v_j = 3^{j-1} v_{dc} \end{cases} \tag{4}$$

The maximal output voltages of these *n* level-inverters are,

$$\text{For} j = 1,2,\ldots.n, V_{out}^{max} = \begin{cases} (2^n - 1) v_{dc} if v_j = 2^{j-1} v_{dc} \\ \left(\frac{3^n - 1}{2}\right) v_{dc} if v_j = 3^{j-1} v_{dc} \end{cases} \tag{5}$$

3.2 Model of PV Array

In this model, a series resistance is called a PV cell, and the current source is parallel with a diode. The PV cell equivalent circuit is depicted in Figure 2. The following equation is shown as the basic current equation:

$$I = I_{pv,CELL} - I_{0,CELL} \left\{ exp \frac{QV}{AKt} - 1 \right\} \tag{6}$$

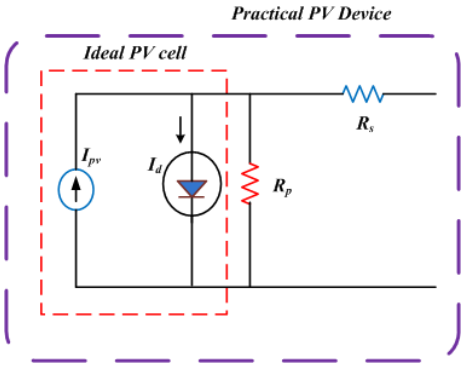

Fig. 2. PV cell equivalent circuit

Here, *K* as Boltzmann-constant, $I_{pv,\,CELL}$ denotes current is created using the incidence light, cell the leakage current of the diode, *Q* as the charge of electron, diode idealist constant is *A, t* as the temperature of PN junction.

$$I = I_{pv} - I_o\left\{\exp\left(\frac{v+R_S I}{v_T A}\right) - 1\right\} - \frac{v+R_S I}{R_p} \tag{7}$$

$$I_{pv} = \left(I_{pv,N} + k_1 \Delta t\right)\frac{g}{gN} \tag{8}$$

Many photovoltaic cells are attached in parallel and series and connection, consisting of a PV array [38].

3.3 Design of Grid-tied PV System Control of Reactive and Active

The 3-phase grid current is given to the proposed method to generate the needed reference of current and voltage. The grid and reference current is changed from the reference frame of abc to dq. The proposed technique is then used to build the proportional integral controller using the dq components and deliver the control signals. While using pulse width modulation, the switching signal of Cascaded MLI is created. The control architecture of dq with active and reactive control action is displayed in Figure 3.

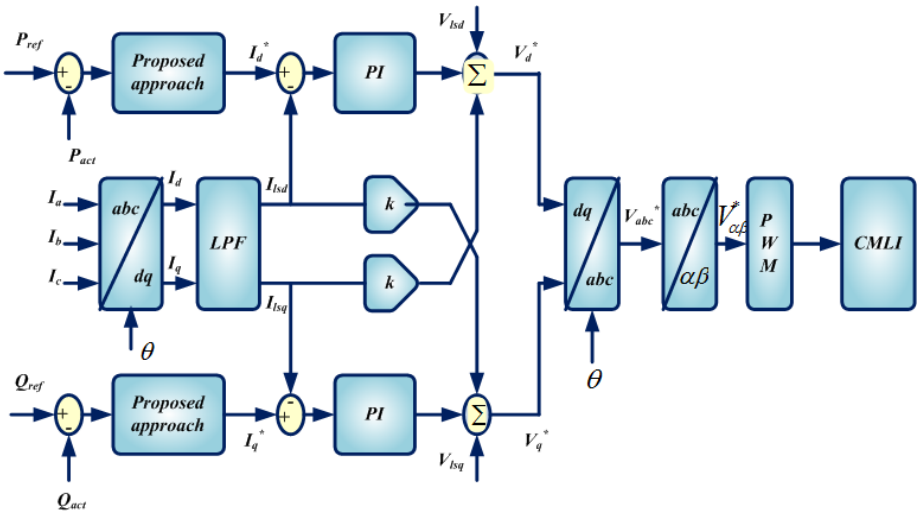

Fig. 3. Control architecture of dq with active and reactive control action

3.4 Control Structures for Grid-tied PV System

The DC manages the power factor to AC converters by injecting sinusoidal current into the grid. Consequently, the inverter transforms the power of PV generators from DC to AC for grid injection. The PV system is the crucial element, and its control is attached to the grid. There are two important parts to the control.

1. MPP controller, whose primary function is to maximise power extraction from the input source,

2. The regulator of the Inverter assurances the dynamic and receptive power control created to the lattice, the voltage control in DC-link, synchronisation with the grid and quality of injected power.

The inverter's control strategy primarily consisted of two cascaded loops. The grid current is typically controlled through a quick internal current loop, and an external voltage loop regulates the DC-connection voltage. The ongoing circle is liable for power quality issues and current security; hence, symphonious remuneration and elements are the significant features of the ongoing regulator. The voltage controller of the DC connection was made to balance the system's power flow. In most cases, this external controller's design aims to ensure optimal stability and regulation in systems with slow dynamics. The stability time of this voltage loop is intended to be five to twenty times longer than that of the internal current loop. It is possible to think of the internal and external loops as decoupling; As a result, the voltage controller is not designed with the transfer function of the current control loop. In some works, instead of using a current loop, the inverter's control depends on the loops of inner power and cascaded DC-link voltage, allowing indirect control of the grid-injected current.

3.5 Eleven-Level Inverter Circuit and Operation

Figure 4 specifies the Power supply for an inverter with 11 levels. The power supply for an inverter with 11 levels is made up of dc link sources$DG_1, DG_2, DG_3, DG_4 and DG_5$ all over the connected dc source. The voltages are combined to create the 11-level voltages using freewheeling diodesD_1, D_2, D_3, D_4, D_5 and power switches of semiconductor S_1, S_2, S_3, S_4, S_5. Moreover, a front circuit made up of power switches, S_1', S_2', S_3', S_4' as well as a coupled inductor attached to the load circuit, is added. This front circuit also comprises a traditional two-level VSI circuit.

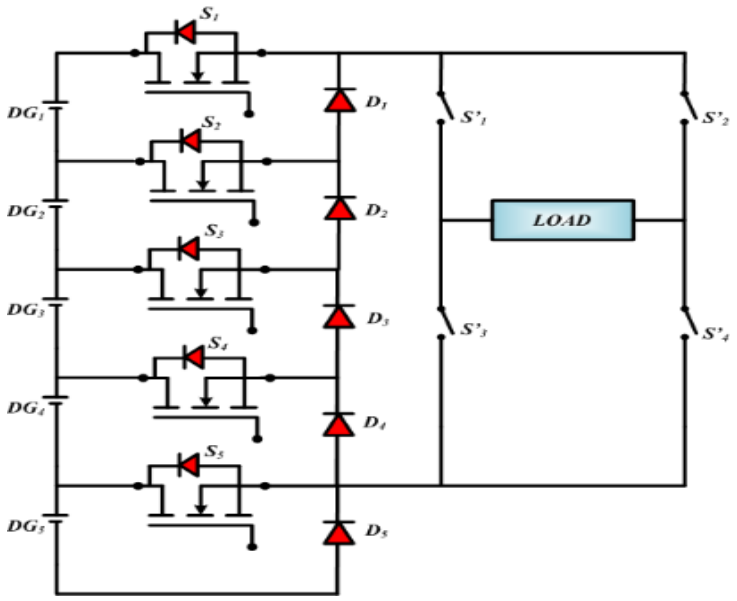

Fig. 4. Power supply for an inverter with 11 levels

3.6 Harmonic Distortion of Current and Voltage

The power system generates harmonics, which results in the nonlinear components of passive and active. The harmonic performance of the bus system is assessed using the total HD of the current

and voltage. The voltage of Total HD is defined as the difference between the power of the fundamental voltage frequency and the sum of every harmonic-voltage element.

$$TVHD = \frac{100\times\sqrt{v_{rms}^2 - v_{frms}^2}}{v_{frms}} \tag{9}$$

$$TIHD = \frac{100\times\sqrt{i_{rms}^2 - i_{frms}^2}}{i_{frms}} \tag{10}$$

where, TVHD, $TIHD$ denotes total-voltage and current-HD, v_{frms} , i_{frms}as the basic frequency of voltage and current,v_{rms} , i_{rms} as components of harmonic voltage and current.

4. The Proposed AHO-SNN Based Multilevel Inverter To lessen the THD in Smart Grid

This manuscript proposes a hybrid technique for reducing the total harmonic distortion in SG. In this, the photovoltaic is the source and utilises the cascaded MLI to lessen the harmonics. The proposed method lessens the difference in the system parameter and external disturbance to meet the system's load demand. As a result, the specifications of the proposed strategy are as follows:

4.1 The Proposed Archerfish Hunting Optimizer

Archerfish Hunting Optimizer (AHO) is a global optimisation that minimises real-world situations' objective functions to arrive at a numerical or analytical solution. It is related to the behaviour of jumping and shooting of archerfish to chase aerial insects. Meta-heuristics are optimisation techniques derived from nature. Exploration and exploitation are the two primary components of metaheuristic algorithms. Global optimisation or diversification is two names for exploration. Local optimisation or intensification of the exploit is the term used. Metaheuristic algorithms can find new search space regions thanks to the exploration and avoid becoming stuck in local optimums. In order to obtain the optimal answer, the exploitation allows meta-heuristic methods to view the specific location. They quickly and numerically solve optimisation issues with solutions close to the ideal. It is based on how archerfish search for flying insects by firing and jumping. Figure 5 depicts the Flowchart of the Archerfish Hunting Optimizer.

Step 1: Initialisation
Initialise the input parameters of the systems, such as dc link voltage, load current, gain parameters of PI controller, PV voltage, iteration and constraints.
Step 2: Random Generation
Generate the input parameters in the form of the matrix at random.

$$X = \begin{bmatrix} (I_{lo}, v_{DC}, v_{PV}, K_p, K_i)^{11} & \cdots & \cdots & (I_{lo}, v_{DC}, v_{PV}, K_p, K_i)^{1N} \\ (I_{lo}, v_{DC}, v_{PV}, K_p, K_i)^{21} & \cdots & \cdots & (I_{lo}, v_{DC}, v_{PV}, K_p, K_i)^{2N} \\ \vdots & \vdots & \vdots & \vdots \\ (I_{lo}, v_{DC}, v_{PV}, K_p, K_i)^{m1} & \cdots & \cdots & (I_{lo}, v_{DC}, v_{PV}, K_p, K_i)^{MN} \end{bmatrix} \tag{11}$$

Here *X* is the random generation and *I*, K_p, K_i are the gain parameters of the proposed system.

Step 3: Fitness calculationEvaluate the fitness based on the objective function, and it is calculated as,

$$f = MIN(THD) \tag{12}$$

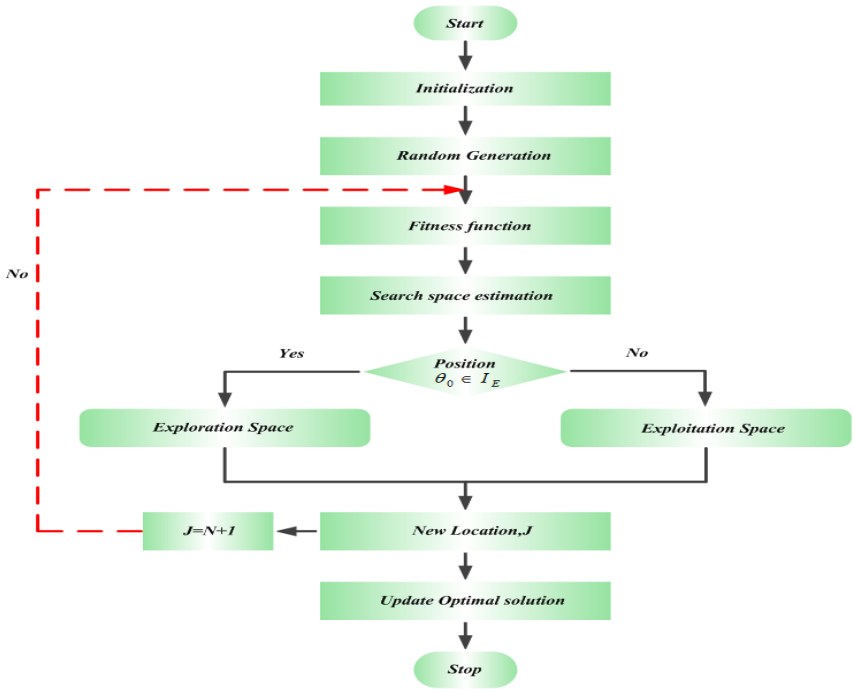

Fig. 5. Flowchart of Archerfish Hunting Optimizer

Step 4: Search Space Estimation
Consider an archerfish-filled search space in dimension *d*. The locations of archer-fish *I* in the iteration *T* is shown below, and the flock size, or number of archerfish, is *n*.

$$Y^{(I,T)} = (Y_1, Y_2, \ldots . Y_d) \tag{13}$$

The entries of each $Y^{(I,T)}$ contains a range of permitted values: that is, $Y^{(I,T)} = \left(Y_J\right) \in \left[Y_J^{MIN}, Y_J^{MAX}\right]$, where, $J \in \{1, \ldots\ldots, d\}$ and $I \in \{1, \ldots\ldots, n\}$.

Step 5: Exploration of Search Space
Provided that the air friction is minimal, it is determined by the perception angle θ_0, launch-speed$V$, and the acceleration of gravity. The insect will fall vertically to the water's surface after being shot by an archerfish$K$. An archerfish moves toward its location when it detects the prey's vibrations I , and the location can be analysed using the following equation.

$$Y^{(I,T+1)} = Y^{(I,T)} + E^{-\left\|Y_{PREY}^{(K,T)} - Y^{(I,T)}\right\|^2}\left(Y_{PREY}^{(K,T)} - Y^{(I,T)}\right) \tag{14}$$

Here, $Y^{(I,T+1)}$as the position of the next archer-fish I, $Y^{(I,T)}$Denote the archerfish's present position I, $\|.\|$ as Euclidean distance, $Y_{PREY}^{(K,T)}$ as the location of prey, E is the count of random vectors are created by a uniform distribution that describes the effects of refraction at the interface of air-water, $Y^{(K,T)}$ specifies archerfish position k, and it spots the insect.

$$Y_{PREY}^{(K,T)} = Y^{(K,T)} + \left(0,\ldots,\frac{V^2}{2G} \times sin\,2\,\theta_0,\ldots,0\right) + \varepsilon \quad (15)$$

Step 6: Search Space exploitation
The archerfish jumps on its victim and catches it. Likewise, the movements of archer-fishes are specified using the launch-speed denote V , perceiving-angle as θ_0, and acceleration-of-gravity G, which tells that friction of air is either low or high. An archerfish Imoves toward the target bug when it decides to capture it.

$$Y(I,T+1) = Y^{(I,T)} + E^{-\left\|Y_{PREY}^{(K,T)} - Y^{(I,T)}\right\|^2}\left(Y_{PREY}^{(I,T)} - Y^{(I,T)}\right) \quad (16)$$

$$Y_{PREY}^{(I,T)} = Y^{(K,T)} + \left(0,\ldots,\frac{V^2}{2G} \times sin\,2\,\theta_0,\ldots,\frac{V^2}{2G} \times sin\,2\,\theta_0,\ldots,0\right) + \varepsilon \quad (17)$$

The entry position is given by $\frac{V^2}{2G} \times sin\,2\,\theta_0$ term that is considered as a random number in $\{1,\ldots\ldots,d\}$ range. The fraction $\frac{V^2}{2G}$is exchanged through variableω for simplicity. It specifies the degree to which an archerfish appeals to a certain prey.

Step 7: Stopping Criterion
Verify the stopping criterion, and the procedure halts if the optimum solution is attained. Else, repeat the steps.

4.2 The Proposed Spiking Neural Network (SNN) Based Prediction

Any neural network that incorporates time and neuronal and synaptic states is referred to as a "spiking neural network" (SNN). Particularly, the SNN algorithm automatically adjusts the synaptic weight of the spiking neural model during the learning stage. SNN provides a superior solution model for balancing exploitation and exploration based on various application data. Neural coding is the process by which spike trains indicate data. Methods for encoding real values include rate, temporal, and population encoding. An appropriate temporal neural coding system for sequence modelling and forecasting tasks evaluates the relevant temporal events concealed inside the sequence. It contains time to next-spike and probability-related encoding. It constantly feeds the exact time of spikes for the network. The time series of firing is used to denote the input and output of spiking neurons named spike-train. The possibility of spiking-neuron is the dynamic variable that serves as a vehicle for incorporating the incoming spikes. The new spikes are greater than those, which is already defined as the possibility for net action. If the integral total of the entering spike exceeds the value already defined, the neuron fires the spike. Since SNN is dynamic, it is a crucial attribute for online load forecasting.

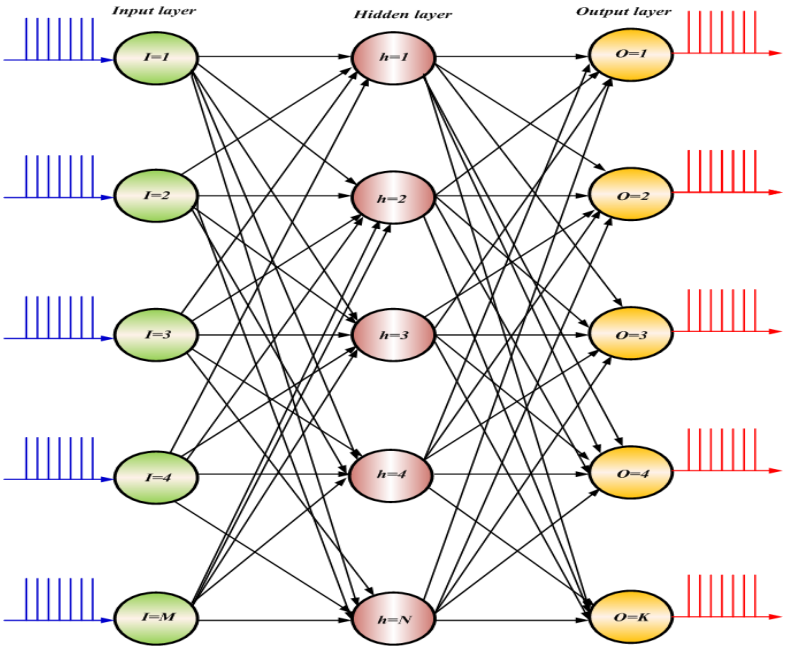

Fig. 6. Spiking Neural Network

5. Result and Discussion

Here, the cascaded MLI performance is based on the simulation outcome. This article used the hybrid AHO-SNN approach to manage solar subsystem power management or maximise energy conversion while lowering THD. Model of Photovoltaic array, multilevel inverter, Circuits and Working of 11-Level Inverter, Voltage and harmonic distortion is the aim of the proposed method. The performance of cascaded MLI is done in the MATLAB platform and compared with the existing methods.

Analysis of irradiation during linear load conditions is displayed in Figure 7. The figure shows that the irradiation is 700 W/m2 for 0 to 0.2 sec, increasing to 900 W/m2. Then it remains steady under 0.2-0.4 sec. Once more, it rises to 1000 W/m2, and it remains fixed. Figure 8 depicts temperature under linear load condition analysis and shows that the temperature value is 20 oC for 0-0.25 sec and rises to 25 °C. Then it remains fixed at 25 °C. Analysis of PV current and Voltage in linear load is displayed in Figure 9. Subplot 9(a) shows PV current linear load, which emerges from 220 A for 0.2 sec. Then the value increases to 280 A at 0.25 times/sec, rises to 283 A for 0.25 to 0.4, rises to 315 A, and stays constant. Subplot 9(b) displays the PV voltage linear. Its photovoltaic voltage is initially 0, rising to 46V from 0.02 to 0.05 and decreasing to 28 V during 0.2 sec. Again it rises to 38 V during 0.24 sec, decreasing to 35 V from 0.24 to 0.43. Again, it rises to 39V. Figure 10 depicts the nonlinear analysis for the PV (a) Current (b) Voltage. Subplot 10(a) displays PV's current nonlinear load. It emerges from 220 A for 0.2 sec and increases to 280 A at 0.25 times/sec, and it increases 283 A at 0.25 to 0.4 and rises to 315 A and stays constant. Subplot 10(b) displays PV voltage nonlinear load. Initially, it starts at 0 and rises to 46V during 0.02 to 0.05 sec, and it decreases to 28 V during 0.2 time/sec; again, it rises to 38 V during 0.24 sec and decreases 35 V during 0.24 to 0.43; again, it rises to 39V. Analysis of the current (a) linear load and (b) nonlinear load is displayed in Figure 11. Subplot 11(a) displays the Current linear load. From 0 to 0.2 sec, the current waveform is 0 to 150 A, drops to -150 A, rises to 220A, and drops to -220 A for 0.22 to 0.4 times/sec. From -250A to 250A, the voltage value continuously differs. Subplot 11(b) depicts the current nonlinear. From 0 to 0.2 times/ sec, the current waveform is 0 to 150 A, drops to -150 A, rises to 220A, and drops to -220 A

for 0.22 to 0.4 times/sec. From -250A to 250A, the voltage value continuously differs. Analysis of load-current (a) linear-load, (b) nonlinear-load is shown in Figure12. Subplot 12(a) shows the load current linear load. It is varied from 0 to 1.50 A, rising from -2.50A to 2.50A at 0.01 to 0.2 sec and from -3A to 3A, the value rises at 0.22 to 0.4 sec. From -4A to 4A, the voltage value continuously differs. Subplot 12(b) shows the load current nonlinear load. It is varied from 0 to 1.50 A, and it rises from -2.50A to 2.50A for 0.01 to 0.2 sec and from -3A to 3A, the value rises at 0.22 to 0.4 sec. The voltage value continuously varies from -4A to 4A. Analysis of inverter voltage is shown in Figure 13. The voltage is initially 0 and increases -1440V to 140V for 0 to 0.2 time/sec. Again, it increases from -200V to 200V for 0.23 to 0.4 time/sec. Again it increases -from 230V to 230V for the remaining period. Analysis of inverter voltage (a) linear load and (b) nonlinear load is displayed in Figure 14. Subplot 14(a) depicts the inverter voltage linear load. It varies from 0 to 190 V, drops -190V from 0 to 0.2time/sec, and increases from -250 V to 250V during the period of 0.2 to 0.4 time/sec. The voltage value continuously differs from -300 to 300 V. Subplot 14(b) depicts the inverter voltage nonlinear load. It varies from 0 to 190 V and drops -190V from 0 to 0.2time/sec, increasing from -250 V to 250V during 0.2-0.4 sec. From -300 to 300 V, the voltage value continuously differs. Analysis of inverter voltage phase A and Inverter voltage phase A zoom is shown in Fig 15. Subplot 15(a) is inverter voltage phase A, which is initially 0, and the voltage increases to 98V and decreases to 110V. Again it increases from -100V to 100V, and it is continuously for the period of 0.04 to 0.02 time/sec, again it increases from -200V to 200V for the period of 0.22 to 0.4 time/sec, again it increases from -230V to 230 V for the remaining time. Subplot 15(b) is inverter voltage phase A zoom, voltage initially -35 and increases -145V to 145V for the time period of 0.103 to 0.143 time/sec and is returned to the initial. Analysis of load voltage linear load and load voltage nonlinear load is shown in Figure 16. Subplot 16 (a) depicts load voltage linear load. from 0 to 0.21 sec, The voltage of the load is severely distorted because of the linear load situation, and again the value varies from -210 to 210 V, increases to -300 to 300 V during 0.22 to 0.41 sec, and from -380 to 380 V, the value varies. Subplot 16(b) depicts load voltage nonlinear load, the 0 to 0.21 sec, the voltage level is -15V to 15, and it rises -22V to 22 V during 0.22 to 0.0.4 time/sec. From -25 V to 25V, it is varied.

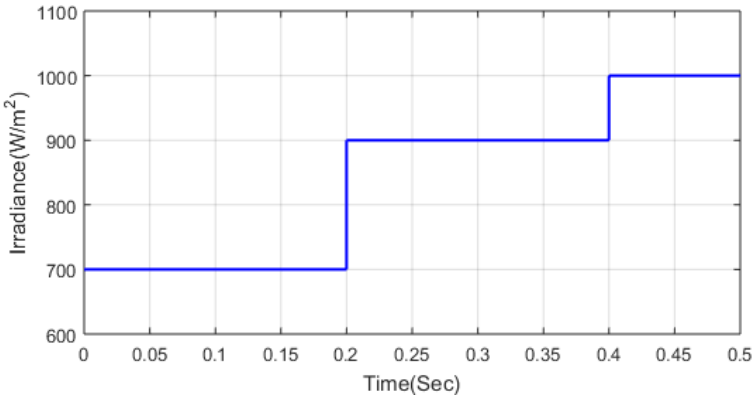

Fig. 7. Analysis of Irradiance during linear load condition

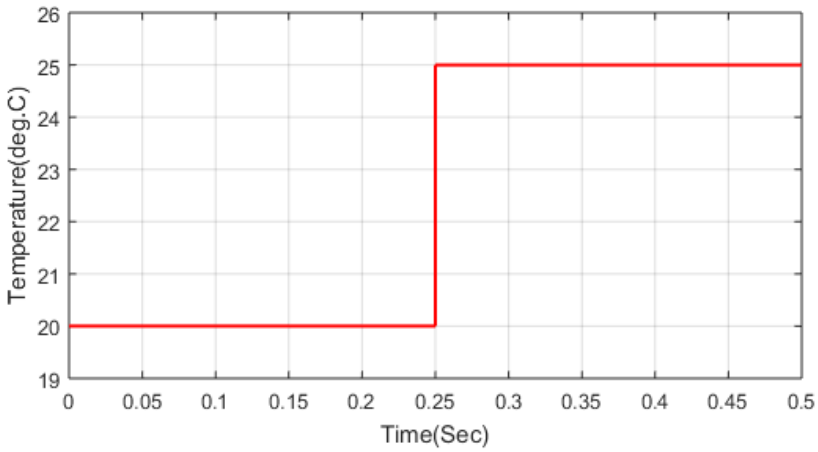

Fig. 8. Temperature during linear load condition analysis

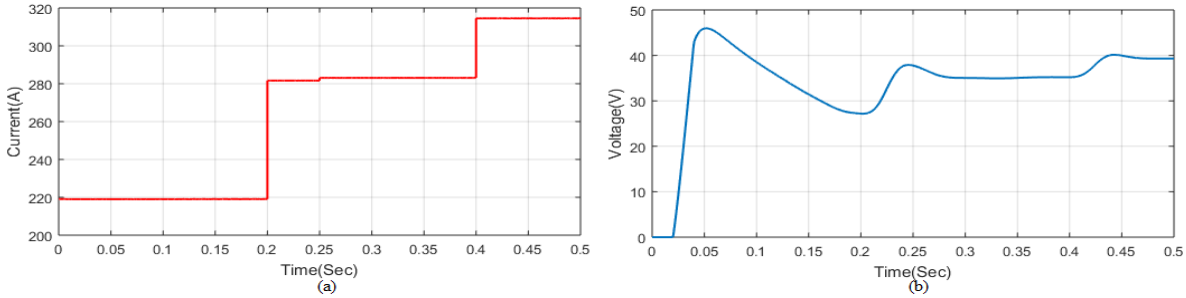

Fig. 9. Analysis of the linear load for the PV (a) Current (b) Voltage

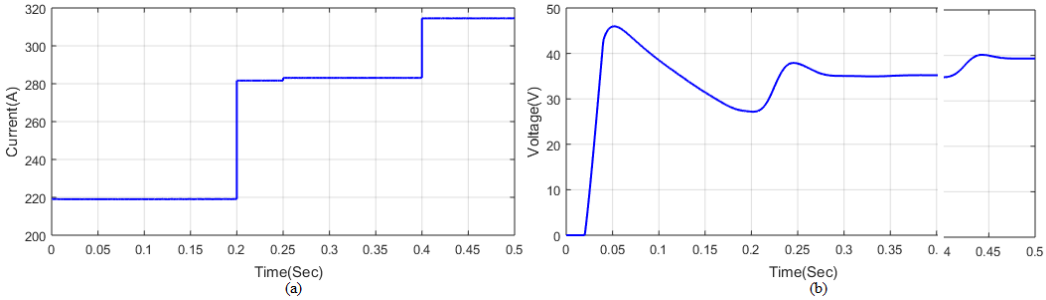

Fig. 10. Analysis of nonlinear for the PV (a) Current (b) Voltage

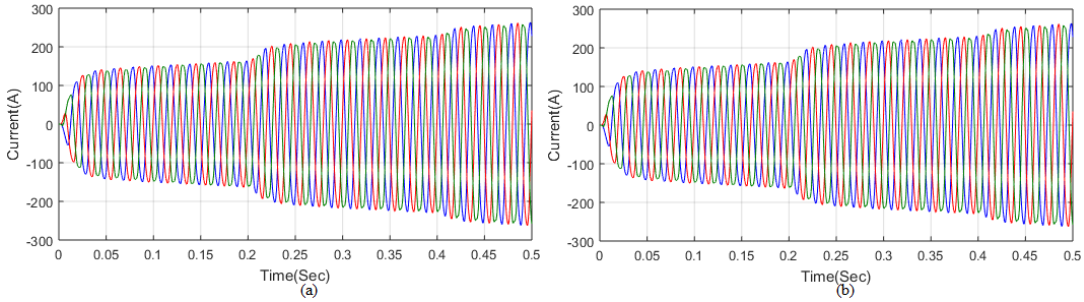

Fig. 11. Analysis of the current (a) linear load, (b) nonlinear-load

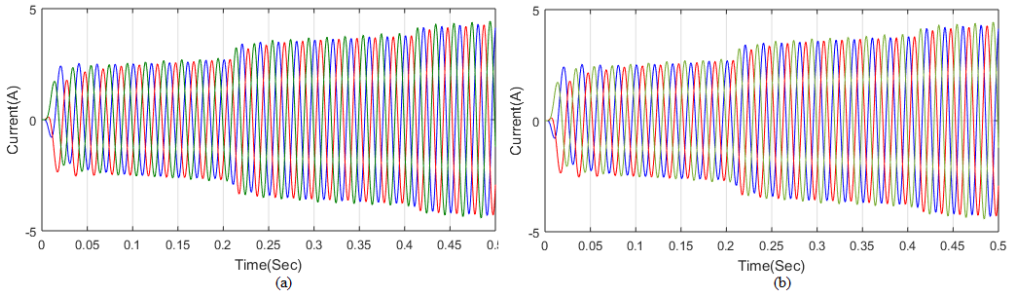

Fig. 12. Analysis of load-current (a) linear-load, (b) nonlinear-load

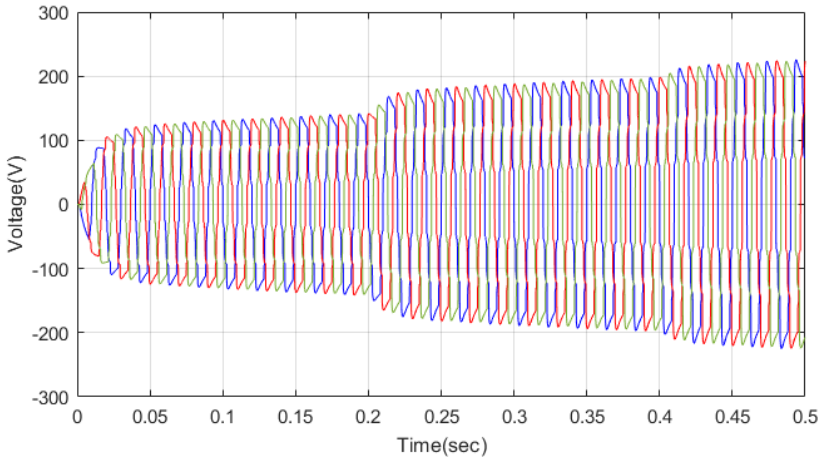

Fig. 13. Analysis of inverter voltage

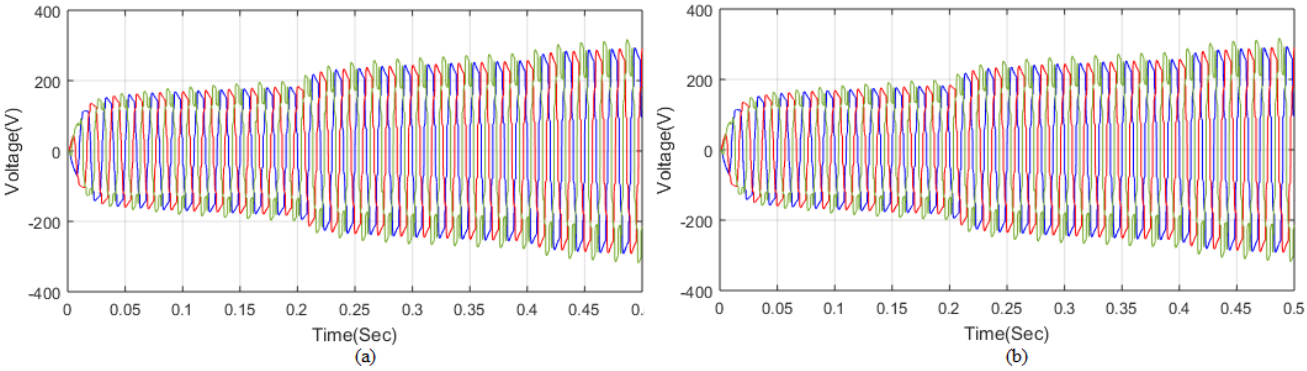

Fig. 14. Analysis of inverter-voltage (a) linear-load, (b) nonlinear-load

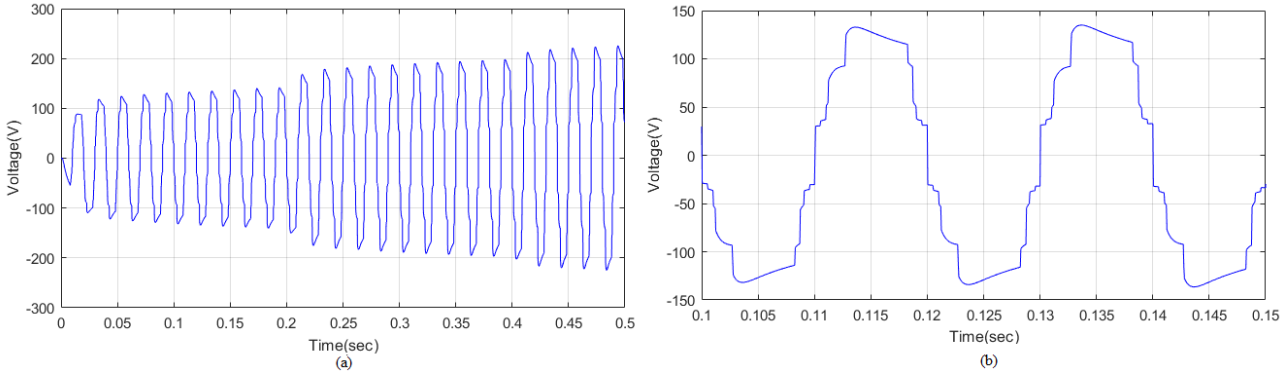

Fig. 15. Analysis of inverter voltage phase A and Inverter voltage phase A zoom (a) Inverter voltage phase A (b) Inverter voltage phase A zoom

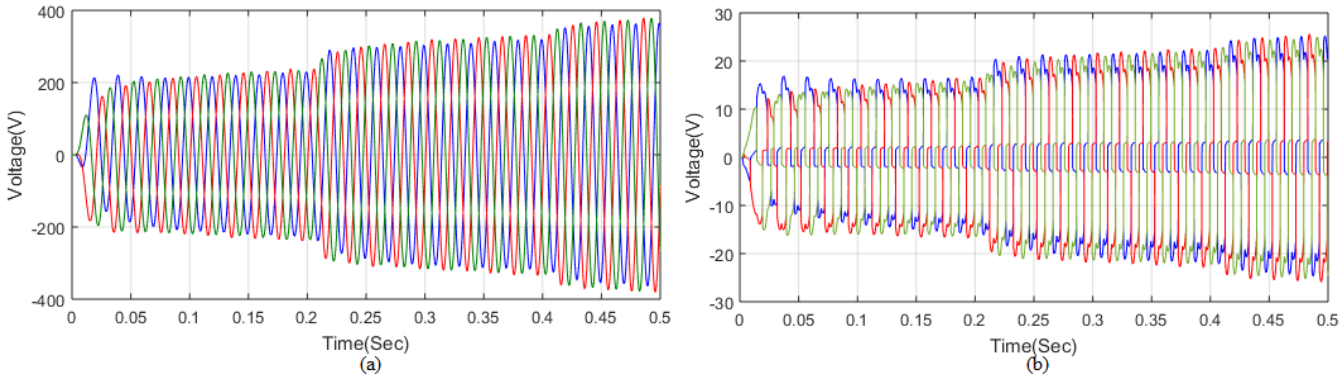

Fig. 16. Analysis of load-voltage (a) linear-load, (b) nonlinear-load

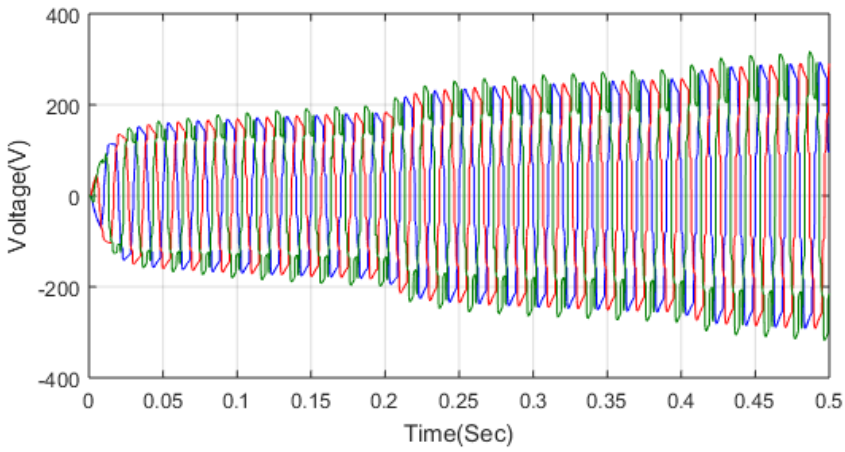

Fig. 17. Analysis of Inverter voltage linear load ANFIS

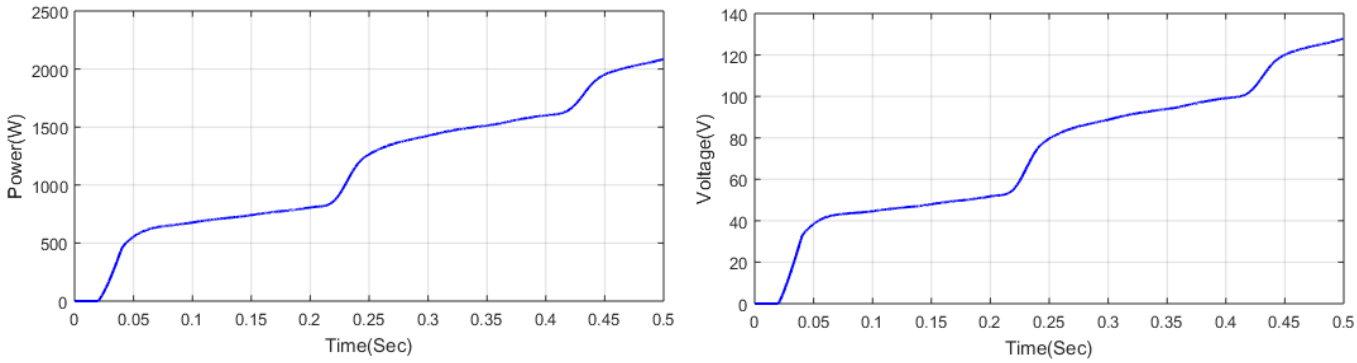

Fig.18. Analysis of Load active power (a) linear load, (b) nonlinear load

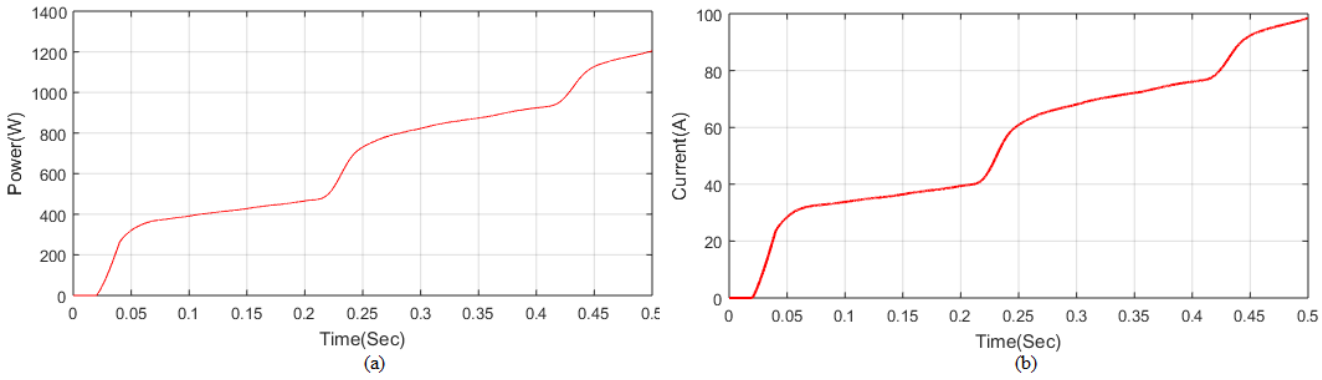

Fig. 19. Analysis of reactive load power (a) linear load, (b) nonlinear load

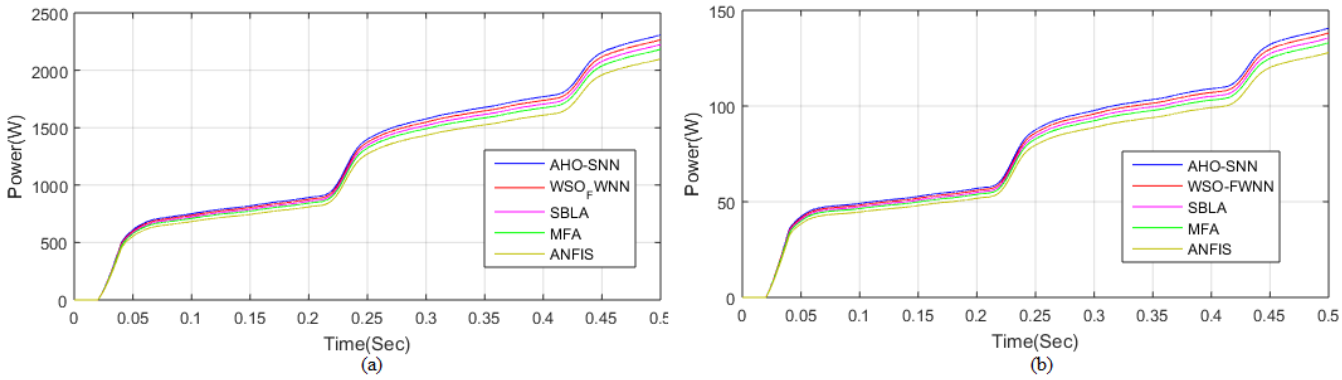

Fig. 20. Comparison of Load active power (a) linear-load COMP (b) nonlinear-load COMP with existing methods

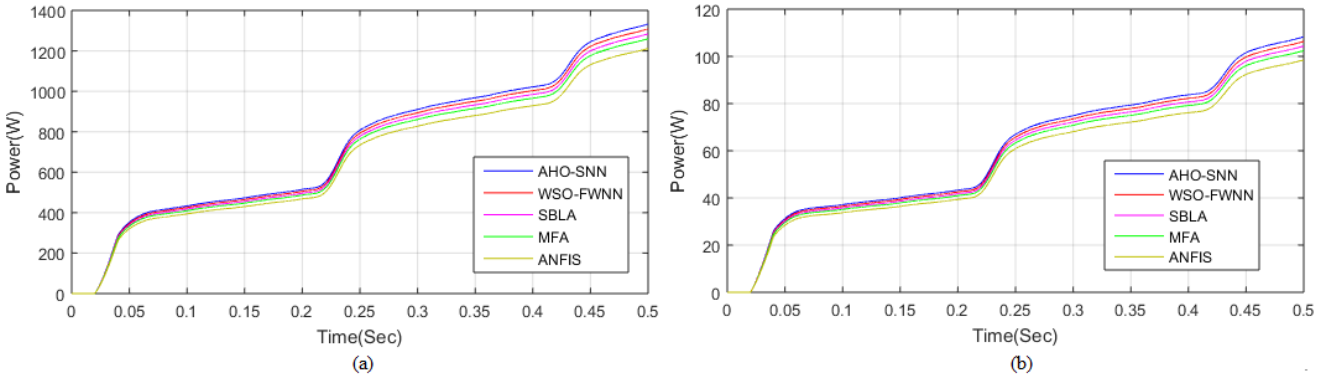

Fig. 21. Comparison of Load reactive power (a) linear-load COMP, (b) nonlinear-load COMP

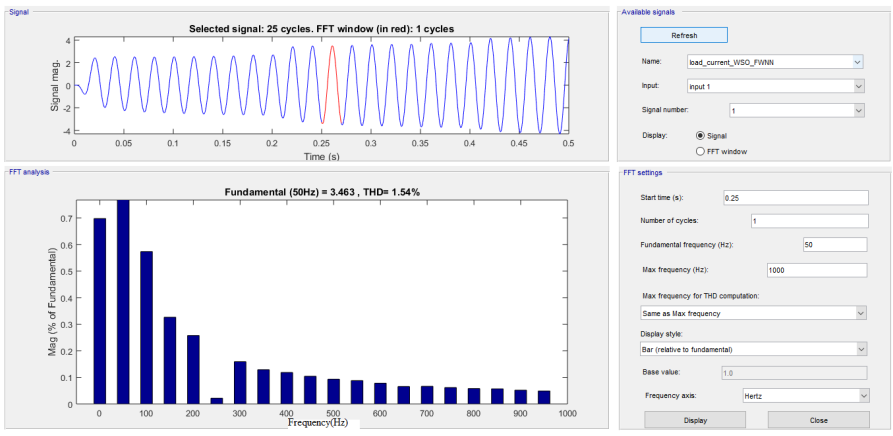

Fig. 22. THD Analysis based on nonlinear load

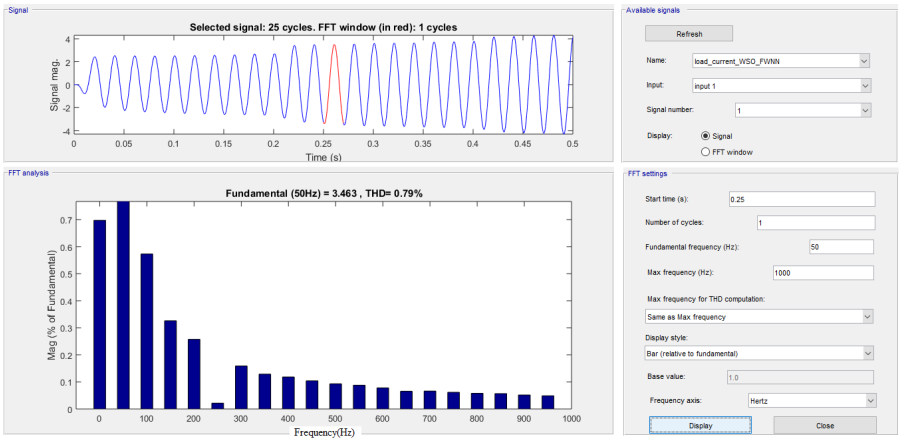

Fig. 23. THD Analysis based on linear load

Table 1
Switch states of multilevel inverter

State	Switches states									Output Voltage
	S1	S2	…	Sn-1	Sn	$S_1^{'}$	$S_2^{'}$	$S_3^{'}$	$S_4^{'}$	
1	0	0	…	0	0	1	0	1	0	0
2	1	0	…	0	0	1	0	0	1	V1
3	1	0	…	0	0	0	1	1	0	-V1
4	0	1	…	0	0	1	0	0	1	V2
5	0	1	…	0	0	0	1	1	0	-V2
⋮	⋮	⋮	⋮	⋮	⋮	⋮	⋮	⋮	⋮	⋮
2n	0	0	…	0	1	1	0	0	1	Vn
2n+1	0	0	…	0	1	0	1	1	0	-Vn
2n+2	1	1	…	0	0	1	0	0	1	(V1+V2)
2n+3	1	1	…	0	0	0	1	1	0	-(V1+V2)
⋮	⋮	⋮	⋮	⋮	⋮	⋮	⋮	⋮	⋮	⋮
2(n+1)-2	1	1	…	1	1	1	0	0	1	(V1+…+Vn)
2(n+1)-2	1	1	…	1	1	0	1	1	0	-(V1+…+Vn)

Table 2
Comparison of THD linear and nonlinear load of proposed and existing approaches

Solution approach	THD%	
	Nonlinear load	Linear load
Proposed	1.54%	0.79%
WSO	1.55%	0.81%
SBLA	1.58%	0.83%
MFA	1.59%	0.85%
ANFIS	1.60%	0.87%

Analysis of inverter voltage linear load ANFIS is depicted in Figure 17. From -200 to 200V, the voltage varies from 0 to 0.2time/sec, rising from -280V to 280V at 0.22 to 0.4time/sec. Then it is varied from -360V to 360V. Analysis of Load active power (a) linear load, (b) nonlinear load is displayed in Figure 18. Subplot 18 (a) depicts the load active power linear load. Initially, it remains fixed at 0 to 0.02 sec, and the load power varies from 0 to 2000W at 0.02 to 0.5 time/sec. Subplot 18(b) shows the load active power nonlinear load. Initially, it remains fixed at 0 to 0.02 sec and is varied from 0 to 123V at 0.02 to 0.5 time/sec. Analysis of reactive load power (a) linear load and (b) nonlinear load is displayed in Figure 19. Subplot 19(a) is load reactive power linear load. The power starts at 0, rises to 450W for 0.02 to 0.22 time/sec, and increases to 930W from 0.23 to 0.42 time/sec. Again it increases. Subplot 19(b) depicts load reactive power nonlinear load.

The power starts at 0 and increases to 40A for 0.03 to 0.22time/sec, and it increases to 78A under 0.25 to 0.43 sec. and again rises to 99A. Comparison of Load active power (a) linear load COMP (b) nonlinear load COMP with existing methods is shown in Figure20. Subplot 20(a) depicts a Comparison of Load active power linear load COMP. It initially starts at 0, increasing 800W under 0.03 to 0.23sec and increasing 1700W from 0.25 to 0.43. Again, it increases by 2300W. In Load active power linear load COMP, the proposed method is 2300W, and the existing WSO-WNN, SBLA, MFA, and ANFIS methods are 2250W, 2200W, 2150W, 2100W Subplot 20(b) shows a Comparison of nonlinear load COMP. The proposed method starts at 0, increasing 800W from 0.03 to 0.23 time/sec and 1700W from 0.25 to 0.43. Again, it increases by 110W. In Load active power linear load COMP, the proposed method is 145 W, and the existing WSO-WNN, SBLA, ANFIS, and MFA methods are 140W, 135W, 130W, and 125W. A comparison of Load reactive power (a) linear load COMP and (b) nonlinear load COMP is shown in Figure 21. Subplot 21(a) shows Load reactive power linear load COMP. Initially, it starts at 0, and it increases 550W during 0.03 to 0.23 time/sec, and it increases 1130W from 0.25 to 0.43 again, it increases 1350W. In Load active power linear load COMP, the proposed method is 1350W, and the existing WSO-WNN, SBLA, MFA, and ANFIS methods are 1350W, 1300W, 1250W, 1200W Subplot 21(b) displays Load reactive power nonlinear load COMP. Initially, it starts at 0, increasing to 45W during 0.03 to 0.23 time/sec, and increasing to 85W during 0.25 to 0.42 sec. Again, it rises to 110W. In Load active power linear load COMP, the proposed method is 110 W and the existing WSO-WNN, SBLA, MFA; ANFIS methods are 108W, 105W, 100W, and 199W. THD Analysis based on nonlinear load is shown in Figure 22. The fundamental frequency is 3.463Hz, and the THD level is 1.54%. THD Analysis based on linear load is shown in Figure 23. The frequency is 3.463Hz, and the THD level is 0.79%.

6. Conclusion

It can be concluded that the minimisation of total harmonic distortion in smart utility. The proposed method is combined with the cascaded MLI, and it is utilised to lessen the total harmonic of the system. The modelling of Cascaded MLI is analysed to achieve the optimum control signal of the proposed controller. The Cascaded MLI method is analysed with fewer sources, diodes, and switches. The proposed method strictly prohibits the differences in Cascaded MLI's output voltage. The AHO method is executed to create the control signals of the Cascaded MLI, and that control signal is optimally predicted by the SNN method. The proposed method is implemented in the MATLAB site, and its performance is compared with existing methods. Numerous situations, including optimal and random scheduling and an elaborate AHO algorithm, are used to examine the proposed technique. The results conclude that the proposed approach based on THD is less compared to existing methods. The proposed method analysed linear load irradiation, nonlinear load irradiation, temperature change, load reactive power linear load, inverter voltage linear load and load reactive-power nonlinear load. Here, the parameters like current, voltage, reactive and active power, temperature and irradiation are analysed to evaluate the system's effectiveness. The simulation result shows that the THD of the proposed method is 0.79%, and the existing WSO, FWNN, SBLA, MFA, and ANFIS methods become 0.81%, 0.83%, 0.85%, 0.87% for both proposed and existing examined. The proposed method has been demonstrated to have less loss than the existing one.

References

[1] Hasanpour, Sara, Yam P. Siwakoti, Ali Mostaan, and Frede Blaabjerg. "New semiquadratic high step-up DC/DC converter for renewable energy applications." *IEEE Transactions on Power Electronics* 36, no. 1 (2020): 433-446. https://doi.org/10.1109/TPEL.2020.2999402

[2] Golestan, Saeed, Josep M. Guerrero, Juan C. Vasquez, Abdullah M. Abusorrah, and Yusuf Al-Turki. "Harmonic linearization and investigation of three-phase parallel-structured signal decomposition algorithms in grid-connected applications." *IEEE Transactions on Power Electronics* 36, no. 4 (2020): 4198-4213. https://doi.org/10.1109/TPEL.2020.3021723

[3] Ghasemi, Mohamad Amin, Hossein Mohammadian Foroushani, and Frede Blaabjerg. "Marginal power-based maximum power point tracking control of photovoltaic system under partially shaded condition." *IEEE Transactions on Power Electronics* 35, no. 6 (2019): 5860-5872. https://doi.org/10.1109/TPEL.2019.2952972

[4] Huang, Zhengrong, Qiang Li, and Fred C. Lee. "Critical-conduction-mode-based soft-switching modulation for three-phase PV inverters with reactive power transfer capability." *IEEE Transactions on Power Electronics* 35, no. 6 (2019): 5702-5713. https://doi.org/10.1109/TPEL.2019.2951130

[5] Dehghani Tafti, Hossein, Ali Iftekhar Maswood, Georgios Konstantinou, Josep Pou, and Pablo Acuna. "Active/reactive power control of photovoltaic grid-tied inverters with peak current limitation and zero active power oscillation during unbalanced voltage sags." *IET Power Electronics* 11, no. 6 (2018): 1066-1073. https://doi.org/10.1049/iet-pel.2017.0210

[6] Liu, Qing, Tommaso Caldognetto, and Simone Buso. "Review and comparison of grid-tied inverter controllers in microgrids." *IEEE Transactions on Power Electronics* 35, no. 7 (2019): 7624-7639. https://doi.org/10.1109/TPEL.2019.2957975

[7] Errouissi, Rachid, and Ahmed Al-Durra. "A novel control technique for grid-tied inverters considering unbalanced grid voltage conditions and control input saturation." *IEEE Transactions on Sustainable Energy* 10, no. 4 (2018): 2223-2234. https://doi.org/10.1109/TSTE.2018.2883863

[8] Sang, Shun, Ning Gao, Xu Cai, and Rui Li. "A novel power-voltage control strategy for the grid-tied inverter to raise the rated power injection level in a weak grid." *IEEE Journal of Emerging and Selected Topics in Power Electronics* 6, no. 1 (2017): 219-232. https://doi.org/10.1109/JESTPE.2017.2715721

[9] Huang, Xin, Keyou Wang, Bo Fan, Qinmin Yang, Guojie Li, Da Xie, and Mariesa L. Crow. "Robust current control of grid-tied inverters for renewable energy integration under non-ideal grid conditions." *IEEE Transactions on Sustainable Energy* 11, no. 1 (2019): 477-488. https://doi.org/10.1109/TSTE.2019.2895601

[10] Komeda, Shohei, and Yoshiya Ohnuma. "An Isolated Single-Phase AC-DC Converter basedon a Dual Active Bridge Converter and an Active Energy Buffer Circuit." In *2021 IEEE 30th International Symposium on Industrial Electronics (ISIE)*, pp. 1-6. IEEE, 2021. https://doi.org/10.1109/ISIE45552.2021.9576405

[11] Geng, Yiwen, Ke Yang, Zou Lai, Pengfei Zheng, Haiwei Liu, and Renxiong Deng. "A novel low voltage ride through control method for current source grid-connected photovoltaic inverters." *IEEE Access* 7 (2019): 51735-51748. https://doi.org/10.1109/ACCESS.2019.2911477

[12] Sefa, Ibrahim, Saban Ozdemir, Hasan Komurcugil, and Necmi Altin. "An enhanced Lyapunov-function based control scheme for three-phase grid-tied VSI with LCL filter." *IEEE Transactions on Sustainable Energy* 10, no. 2 (2018): 504-513. https://doi.org/10.1109/TSTE.2018.2833809

[13] Sochor, Paul, Nadia Mei Lin Tan, and Hirofumi Akagi. "Low-voltage-ride-through control of a modular multilevel single-delta bridge-cell (SDBC) inverter for utility-scale photovoltaic systems." *IEEE Transactions on Industry Applications* 54, no. 5 (2018): 4739-4751. https://doi.org/10.1109/TIA.2018.2845893

[14] Liu, Qing, Tommaso Caldognetto, and Simone Buso. "Review and comparison of grid-tied inverter controllers in microgrids." *IEEE Transactions on Power Electronics* 35, no. 7 (2019): 7624-7639. https://doi.org/10.1109/TPEL.2019.2957975

[15] Mahrous, E. A., N. A. Rahim, and W. P. Hew. "Three-phase three-level voltage source inverter with low switching frequency based on the two-level inverter topology." *IET Electric Power Applications* 1, no. 4 (2007): 637-641. https://doi.org/10.1049/iet-epa:20060280

[16] Li, Jun, Subhashish Bhattacharya, and Alex Q. Huang. "A new nine-level active NPC (ANPC) converter for grid connection of large wind turbines for distributed generation." *IEEE transactions on Power Electronics* 26, no. 3 (2010): 961-972. https://doi.org/10.1109/TPEL.2010.2093154

[17] Li, Chushan, Shuai Wang, Qingxin Guan, and David Xu. "Hybrid modulation concept for five-level active-neutral-point-clamped converter." *IEEE Transactions on Power Electronics*32, no. 12 (2017): 8958-8962. https://doi.org/10.1109/TPEL.2017.2699948

[18] Guan, Qing-Xin, Chushan Li, Yu Zhang, Shuai Wang, Dewei David Xu, Wuhua Li, and Hao Ma. "An extremely high efficient three-level active neutral-point-clamped converter comprising SiC and Si hybrid power stages." *IEEE Transactions on Power Electronics* 33, no. 10 (2017): 8341-8352. https://doi.org/10.1109/TPEL.2017.2784821

[19] Siwakoti, Yam P., Akshay Mahajan, Daniel J. Rogers, and Frede Blaabjerg. "A novel seven-level active neutral-point-clamped converter with reduced active switching devices and DC-link voltage." *IEEE Transactions on Power Electronics* 34, no. 11 (2019): 10492-10508. https://doi.org/10.1109/TPEL.2019.2897061

[20] Ha, Chin Yee, Terh Jing Khoo, and Jia Xuan Loh. "Barriers to green building implementation in Malaysia: A systematic review." *Progress in Energy and Environment* (2023): 11-21. https://doi.org/10.37934/progee.24.1.1121

[21] Ilham, Zul. "Multi-criteria decision analysis for evaluation of potential renewable energy resources in Malaysia." *Progress in Energy and Environment* 21 (2022): 8-18. https://doi.org/10.37934/progee.21.1.818